

Article

Study on Dynamic Characteristics of Magnetic Coagulation of Fe-Based Fine Particles in Iron and Steel Industry

Dengke Xu ¹ , Zuxiang Hu ^{2,3,*}, Li'an Zhang ¹ and Wenqing Zhang ²

¹ School of Civil Engineering and Architecture, Anhui University of Science and Technology, Huainan 232001, China; dkxu@aust.edu.cn (D.X.); lazhang@aust.edu.cn (L.Z.)

² School of Energy and Safety, Anhui University of Science and Technology, Huainan 232001, China; wqzhang@aust.edu.cn

³ Key Laboratory of Industrial Dust Prevention and Control & Occupational Health and Safety, Ministry of Education, Huainan 232001, China

* Correspondence: zxhu@aust.edu.cn

Abstract: Fine dust, represented by Fe-based fine particles and emitted from the production process of the iron and steel industry, is the primary factor causing many diseases represented by industrial pneumoconiosis, and ultra-low dust emission has always been a thorny problem to be solved urgently. To explore the magnetic coagulation effect of Fe-based fine particles in the magnetic field when removing them from industrial flue gas by the magnetic field effect in the iron and steel industry, using FLUENT software, magnetic dipole force was added between particles through user defined function (UDF) based on the computational fluid dynamics-discrete phase model (CFD-DPM) method so that the collision process of particles was then equivalent to their mutual trapping process. Next, the effects of particle size, particle volume fraction, external magnetic field strength, and particle magnetic susceptibility on the magnetic coagulation process were comprehensively studied. Meanwhile, the proton balance equation (PBE) was solved using the partition method on the basis of the computational fluid dynamics-population balance model (CFD-PBM) to compare the coagulation removal effect under random and aligned orientations of magnetic dipoles, respectively. The results showed that the magnetic coagulation strength under the random orientation of magnetic dipoles was greater than that under the aligned orientation. When the particle size of Fe-based fine particles increased from 0.5 μm to 1.5 μm , the magnetic coagulation coefficient decreased from 0.5414 to 0.2882, and the difference in the removal efficiency under the two different orientations of magnetic dipoles became smaller. When the particle volume fraction increased from 0.01 to 0.03, the magnetic coagulation coefficient increased from 0.2353 to 0.5061, and the difference in the removal efficiency under two orientations was enlarged. When the applied external magnetic field strength increased from 0.5 T to 1.0 T, the magnetic coagulation coefficient increased from 0.3940 to 0.5288, and the magnetic susceptibility increased from 0.0250 to 0.0500, the coagulation coefficient increased from 0.3940 to 0.5288, and the difference under two orientations basically stayed unchanged.

Keywords: Fe-based fine particles; magnetic field effect; magnetic dipole force; magnetic coagulation; removal efficiency



Citation: Xu, D.; Hu, Z.; Zhang, L.; Zhang, W. Study on Dynamic Characteristics of Magnetic Coagulation of Fe-Based Fine Particles in Iron and Steel Industry. *Atmosphere* **2023**, *14*, 1434. <https://doi.org/10.3390/atmos14091434>

Academic Editors: Jianlong Li, Jianwu Chen, Hong Huang and Cuiping Yan

Received: 10 August 2023

Revised: 9 September 2023

Accepted: 11 September 2023

Published: 14 September 2023



Copyright: © 2023 by the authors. Licensee MDPI, Basel, Switzerland. This article is an open access article distributed under the terms and conditions of the Creative Commons Attribution (CC BY) license (<https://creativecommons.org/licenses/by/4.0/>).

1. Introduction

China is in a rapid stage of industrial development, accompanied by deep-seated conflicts and problems such as production overcapacity, serious repeated construction, and increased pressure on industrial environmental protection. As a big steel producer, China has ranked first in the world steel production since 1996 [1]. As a resource-intensive and energy-intensive industry, the iron and steel industry shows a large amount of energy consumption and pollutant emission in the production process. Compared with other industries, it is a typical heavily polluting industry [2,3], becoming one of the key targets of

air pollution control in China. Especially, the emitted fine particles with a diameter less than or equal to $2.5\ \mu\text{m}$ ($\text{PM}_{2.5}$ for short) can be carriers of other pollutants because of their large quantity, slow settling speed, and large specific surface area, having a serious impact on the quality of the atmospheric environment [4]. It is worth noting that $\text{PM}_{2.5}$ is also an important inducement for the development of various respiratory diseases [5]. Therefore, it is urgent to solve the problem of particulate pollutant emission in heavily polluting industries such as the iron and steel industry.

The filter material filtration method has been widely used in the field of industrial flue gas purification by virtue of its high particle trapping efficiency and a wide applicable range of particle sizes [6]. To further improve particle trapping performance, the fiber cross-sectional shape (profiled fiber) [7–9] and fiber diameter [10] can be changed from the fiber level. From the level of filtering media, the internal fiber distribution density [11], fiber axial curvature [12], fiber bending degree [13], fiber arrangement structure [14], and the geometric structure of filtering media can be changed, in which the filtering media mainly include flat plate type [15], fold type [16], and topological structure type [17]. From the level of filter materials, the surface of the traditional filter material can be loaded with nanofibers [18] or the planar filter material can be designed as folded filter material [19]. When the above methods are used for improvement, however, the particles in the range of $0.1\text{--}0.5\ \mu\text{m}$ [20–22] show an unobvious Brownian diffusion effect and inertial collision effect, and thus fine particles escape, a problem that cannot be radically solved yet.

By analyzing the physical properties of the dust produced in the production process, it was found that after the raw Fe ore is crushed and steam-condensed at high temperature, there are many metal components in the particles, and the content of Fe element is much higher than that of other elements [23,24], and Fe magnetic substances such as Fe_3O_4 and Fe_2O_3 are the main components of the dust [25]. Therefore, it can be seen that many easily magnetized Fe-based fine particles are produced in the production process of the iron and steel industry, which can be magnetically coagulated by the magnetic field effect and then removed. In the traditional flow field, the motion state of particles after collision depends on the relative magnitude of drag force, gravity, viscous force (Van der Waals force), and collision elastic force [26]. When $d_p < 30\ \mu\text{m}$, the viscous force, represented by Van der Waals force, is dominant in this region. When particles collide or contact with each other, the collision coagulation effect occurs [27]. When a uniform magnetic field is added to the flow field, the particles in the flow field are not only subjected to drag force and gravity but also to magnetic dipole force before collision. When $d_p < 10\ \mu\text{m}$, the ratio of magnetic dipole force to drag force is less than 1, and the ratio to gravity exceeds the order of magnitude of 10^2 [28]. Although the magnetic dipole force is smaller than the drag force, they are in the same order of magnitude. Before particles collide with each other, the existence of magnetic dipole force accelerates the collision coagulation effect. When particles collide with each other, the colliding particles are subjected to the combined action of five forces: drag force, gravity force, viscous force, collision elastic force, and magnetic dipole force, and the existence of magnetic dipole force enhances the collision coagulation effect. Chinese and foreign scholars have done a lot of research on the magnetic coagulation process of ferromagnetic particles in the magnetic field.

Based on the magnetic dipole theory, Ku [29] analyzed the magnetic potential energy characteristics of magnetic particles in the magnetic field, derived the expression of the interaction force between magnetic particles, and simulated their dynamic characteristics. The results showed that magnetic particles are coagulated along the direction of external magnetic field and arranged in a chain structure. Ke [30] numerically simulated the dynamic characteristics of magnetic particles in vertical and horizontal uniform magnetic fields. The results revealed that the external magnetic field has a significant influence on the dynamic characteristics of magnetic particles, and the particles form some fragmented chains along the flow direction, which are continuously elongated and aligned, and finally approach a stable state. Senkawa [31] studied the magnetic interaction between two magnetic particles and obtained different expressions of the magnetic interaction between two magnetic

particles. Karvelas [32] explored the magnetic coagulation behavior of Fe_3O_4 nanoparticles in a uniform magnetic field, and the results showed that Fe_3O_4 nanoparticles will form a chain structure under the action of the magnetic field. Hleis [25] investigated the particle deposition process in a high-gradient magnetic field. The results showed that under the conditions of low external magnetic field strength and low flow rate, the particles will form chain structures or chain beams on the way to the magnetic filter media. It was found that the ferromagnetic particles in the external magnetic field, no matter whether it is a uniform magnetic field or a gradient magnetic field, will form a chain structure under the action of the magnetic dipole force. In this study, therefore, the dynamic process of ferromagnetic particles coagulated into chains is not discussed, and the magnetic coagulation effect and strength of Fe-based fine particles in a uniform magnetic field were mainly studied.

When the magnetic coagulation dynamic process of Fe-based fine particles was calculated using the CFD-DPM method, the force on the two particles colliding with each other was analyzed, and the particle motion equilibrium equation in the composite field composed of flow field and magnetic field was established. The magnetic coagulation process could be analogized to the trapping process of one particle to another. The magnetic dipole force between particles was added by UDF, and a binary collision model was established for calculation, aiming to explore the effects of particle size, particle volume fraction, external magnetic field strength, and particle magnetic susceptibility on the magnetic coagulation process. To study the effect of the magnetic dipole orientation on magnetic coagulation and removal, moreover, the CFD-PBM method was used to calculate the dynamic process of magnetic coagulation and removal of Fe-based fine particles, and the magnetic coagulation kernel function was added to the PBM module through UDF, and the magnetic coagulation removal effects under random orientation and aligned orientation of magnetic dipoles were compared. This study has certain guiding significance for the subsequent magnetic coagulation removal of Fe-based fine particles.

2. Physical Model and Boundary Conditions

Figure 1 shows the Fe-based fine particle collision model. The collision process of Fe-based fine particles in a uniform magnetic field can be regarded as a particle-to-particle trapping process, as shown in Figure 1a. It can be seen from Figure 1b that the direction of the uniform magnetic field was consistent with the movement speed of the inlet particles, and the gravity was in the $-Z$ axis direction, the model inlet was a velocity inlet with uniform velocity distribution, the model outlet was a free outflow, the air density was 1.225 kg/m^3 , the periphery boundary was set as a wall, and a no-slip boundary condition was adopted for the core particle surface [33]. When the length and height of the calculation domain were greater than 5 times and 1.5 times of the core particle diameter, a stable flow field was formed in the calculation area without affecting the particle trapping efficiency [34,35]. Therefore, the distance from the inlet and outlet of the model to the core particle center was $3.5D$, the width and height were $3D$, and the core particle size was the same as that of the inlet particle.

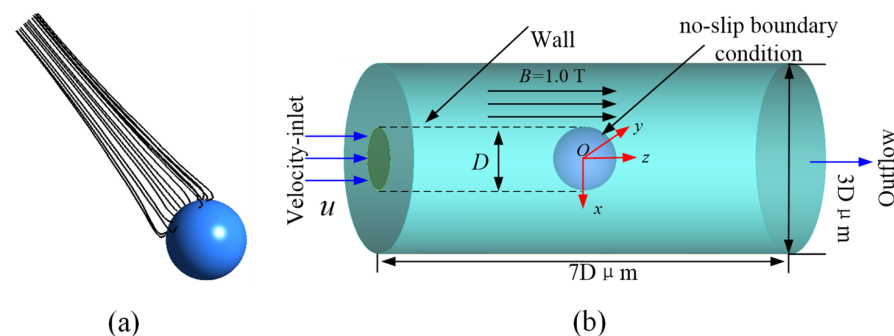


Figure 1. Collision model of Fe-based fine particles in magnetic field: (a) streamlines of particle-to-particle trapping process; (b) physical model of Fe-based fine particles collision.

In addition, taking converter ash and refined ash as examples, Figure 2 shows the magnetic characteristics of Fe-based fine particles emitted during steelmaking in the iron and steel industry. As seen from Figure 2a, Fe-based fine particle XRD testing showed that Fe-based fine particles contained Fe₂O₃, Fe₃O₄ and other ferromagnetic substances, which had the characteristics of easy magnetization in the magnetic field. Figure 2b shows the VSM curve of converter ash and refined ash. The VSM hysteresis loop shows that when the external magnetic field intensity reached 0.5 T, the specific saturation magnetization of converter ash and refined ash was 22.5 emu/g and 3.32 emu/g, respectively. The calculated magnetic susceptibility of the two kinds of dust was 0.1363 and 0.01989, respectively, indicating that the magnetic properties of converter ash are greater than those of refined ash, and it is more easily magnetized in the magnetic field.

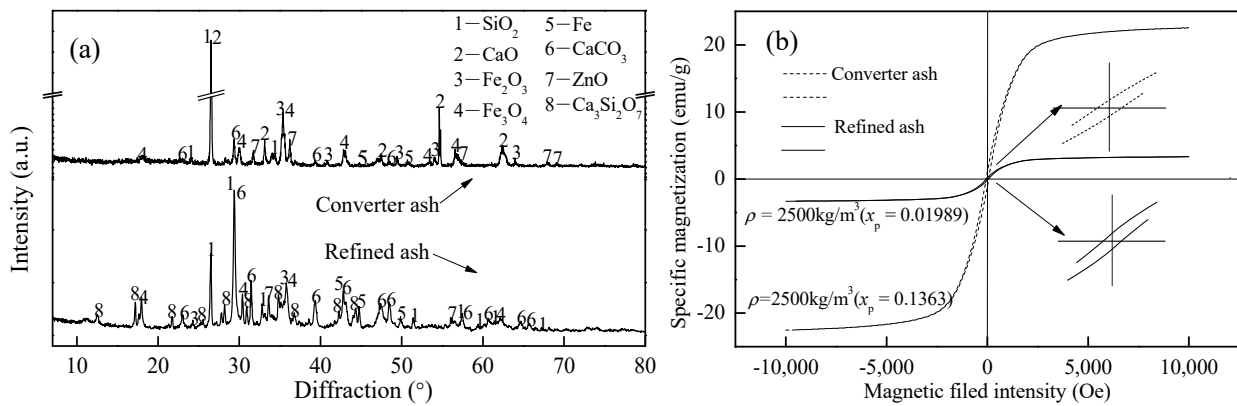


Figure 2. Magnetic characteristics of Fe-based fine particles emitted from iron and steel industries: (a) XRD patterns of converter ash and refined ash; (b) VSM curve of converter ash and refined ash.

3. Numerical Calculation Equations

3.1. Governing Equations for the Fluid Phase

The Euler–Euler double-fluid model was used as the gaseous field model. The Reynolds number was calculated as $Re = ud/\nu < 1$, categorized as a laminar flow ($u = 0.1 \text{ m/s}$, $0.5 \mu\text{m} \leq d \leq 2.5 \mu\text{m}$, $\nu = 15.70 \times 10^{-6} \text{ m}^2/\text{s}$), with the continuity equation and momentum equation as follows [15]:

$$\frac{\partial(\alpha\rho u)}{\partial t} + \nabla \cdot (\alpha\rho u) = 0 \tag{1}$$

$$\frac{\partial(\alpha\rho u)}{\partial t} + \nabla \cdot (\alpha\rho uu) = -\alpha\nabla P + \alpha\rho g + \nabla \cdot \tau - F \tag{2}$$

where α is the volume fraction; ρ is the density of the fluid, kg/m^3 ; u is the velocity of the fluid, m/s ; ∇ is the Hamilton operator; P is the pressure of the grid cell, Pa; τ is the fluid adhesion stress tensor; g is the gravitational acceleration, m/s^2 ; and F is the resultant force on the grid cells, Pa.

3.2. Governing Equations for the Particles

In a gas–solid two-phase flow, the motion of discrete phase particles is described by Newton’s second law, and the motion equilibrium equation of particles is expressed as follows [14]:

$$m_p \frac{d\vec{u}_p}{dt} = \vec{F}_D + \vec{F}_B + \vec{F}_g + \vec{F}_{other} \tag{3}$$

$$\vec{F}_D = m_p \left(\frac{18\mu}{\rho_p d_p^2 C_c} (\vec{u} - \vec{u}_p) \right) \tag{4}$$

$$\vec{F}_B = m_p \left(G_i \sqrt{\frac{\pi S_0}{\Delta t}} \right) \tag{5}$$

$$\vec{F}_g = m_p \left(\frac{\vec{g} (\rho_p - \rho)}{\rho_p} \right) \tag{6}$$

$$Kn = 2\lambda / d_p \tag{7}$$

$$C_c = 1 + Kn \left(1.257 + 0.4e^{-1.1/Kn} \right) \tag{8}$$

$$S_0 = 216\nu k_b T / \pi^2 \rho_p^2 d_p^5 C_c \tag{9}$$

where F_D , F_B , and F_g are respectively the drag force, Brownian force, and gravity, N; m_p is the mass of particles, kg; u_p is the velocity of the particle, m/s; ν is the dynamic viscosity of the fluid, Pa·s; G_i is a Gaussian random function with a mean of 0 and a variance of 1; S_0 is the spectral intensity of noise, m^2/s^3 ; Kn is the particle Knudsen number; C_c is the Cunningham correction factor; d_p is the particle diameter, μm ; k_b is the Boltzmann constant; λ is the average free path of air molecules, nm; ρ_p is the density of particle, kg/m^3 ; F_{other} includes negligible forces, such as pressure gradient force, Bassett force, virtual mass force, and Magnus force, N, and $F_{other} = 0$ by default.

The force of Fe-based fine particles under the action of magnetic dipole force was analyzed, and the force diagram is shown in Figure 3. The motion equilibrium equation of particles is expressed as follows:

$$m_p \frac{d\vec{u}_p}{dt} = \vec{F}_D + \vec{F}_B + \vec{F}_g + \vec{F}_{\text{Magnetic dipole force}} + \vec{F}_{\text{other}} \tag{10}$$

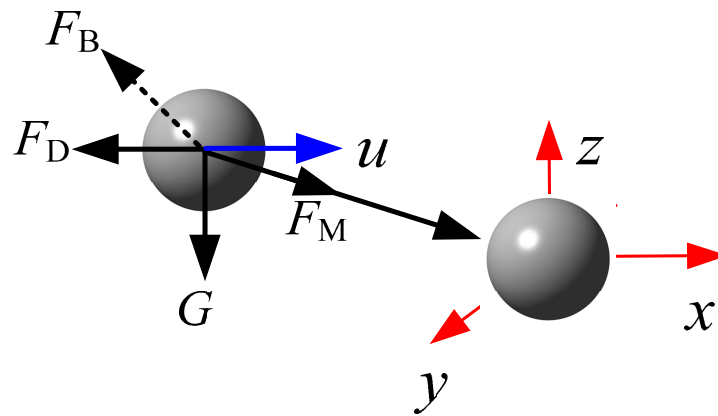


Figure 3. Force diagram of Fe-based fine particles.

(1) Magnetic dipole force in three-dimensional space

In the compound field composed of flow field, magnetic field, and gravity field, Fe-based fine particles will form magnetic dipoles after being magnetized under the action of the uniform magnetic field. The schematic diagram magnetic dipole forces between Fe-based fine particles is shown in Figure 4.

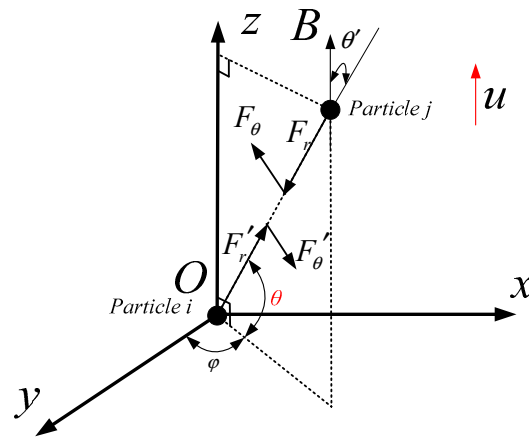


Figure 4. Schematic diagram of magnetic dipole forces between Fe-based fine particles.

The magnetic dipole force between the two particles is decomposed along the radial direction and tangential direction, and the calculation formulas for the radial force F_r' and tangential force F_{θ}' of particle j on particle i are as follows [36]:

$$\begin{cases} F_r' = \frac{3\mu_0 m_i m_j [3\cos\theta'_i \cos\theta'_j - \cos(\varphi_i - \varphi_j)]}{4\pi r^4} \\ F_{\theta}' = -\frac{3\mu_0 m_i m_j \sin(\theta'_i + \theta'_j)}{4\pi r^4} \end{cases} \quad (11)$$

where the permeability of vacuum is $\mu_0 = 1.256 \times 10^{-6} \text{ N/A}^2$; m_i and m_j are the magnetic dipole moment of particle i and j , respectively, $\text{A}\cdot\text{m}^2$; and r is the linear distance between two particles, m . Since the magnetic field is consistent with magnetic dipole moment in direction, $\varphi_i = \varphi_j = \varphi$, $\theta'_i = \theta'_j = \theta'$, and $m_i = 4/3\pi(d_i/2)^3 M_i$, $m_j = 4/3\pi(d_j/2)^3 M_j$, so the calculation formulas for the radial force F_r' and tangential force F_{θ}' of particle j on particle i can be simplified as follows:

$$\begin{cases} F_r' = \frac{\pi\mu_0 m_i m_j d_i^3 d_j^3 (3\cos^2\theta' - 1)}{48r^4} \\ F_{\theta}' = -\frac{\pi\mu_0 m_i m_j d_i^3 d_j^3 \sin 2\theta'}{48r^4} \end{cases} \quad (12)$$

where d_i and d_j are the particle sizes of particle i and j , respectively.

In addition, the saturation magnetization of the two colliding particles is the same; that is, $M_i = M_j = M_p$, and the final calculation formulas for the radial force F_r' and tangential force F_{θ}' of particle j on particle i can be expressed as follows:

$$\begin{cases} F_r' = \frac{\pi\mu_0 M_p^2 d_i^3 d_j^3 (3\cos^2\theta' - 1)}{48r^4} \\ F_{\theta}' = -\frac{\pi\mu_0 M_p^2 d_i^3 d_j^3 \sin 2\theta'}{48r^4} \end{cases} \quad (13)$$

According to Newton's third law, the force action is mutual, and the calculation formulas for the radial force F_r' and tangential force F_{θ}' of particle i on particle j can be expressed as follows:

$$\begin{cases} F_r' = -\frac{\pi\mu_0 M_p^2 d_i^3 d_j^3 (3\cos^2\theta' - 1)}{48r^4} \\ F_{\theta}' = \frac{\pi\mu_0 M_p^2 d_i^3 d_j^3 \sin 2\theta'}{48r^4} \end{cases} \quad (14)$$

When the direction of the uniform magnetic field and inlet particle are parallel along the Z axis, particles attract each other due to the magnetic attraction at $3\cos^2\theta' - 1 > 0$, and particles repel each other due to the magnetic repulsion at $3\cos^2\theta' - 1 < 0$. The radial and

tangential components of the magnetic dipole force under the Cartesian coordinate system are expressed as follows:

$$\begin{cases} F_{M(x)} = F_r \sin \theta \sin \varphi - F_\theta \cos \theta \sin \varphi \\ F_{M(y)} = F_r \sin \theta \cos \varphi - F_\theta \cos \theta \cos \varphi \\ F_{M(z)} = F_r \cos \theta + F_\theta \sin \theta \end{cases} \quad (15)$$

According to $\sin \theta = \sqrt{x^2 + y^2}/r$, $\cos \theta = z/r$, $\sin \varphi = x/\sqrt{x^2 + y^2}$, and $\cos \varphi = y/\sqrt{x^2 + y^2}$, the magnetic dipole force equation under the Cartesian coordinate system is expressed as follows:

$$\begin{cases} F_{M(x)} = \frac{\pi \mu_0 M_p^2 d_i^3 d_j^3 (x^2 + y^2 - 4z^2) \cdot x}{48(x^2 + y^2 + z^2)^{7/2}} \\ F_{M(y)} = \frac{\pi \mu_0 M_p^2 d_i^3 d_j^3 (x^2 + y^2 - 4z^2) \cdot y}{48(x^2 + y^2 + z^2)^{7/2}} \\ F_{M(z)} = \frac{\pi \mu_0 M_p^2 d_i^3 d_j^3 (3x^2 + 3y^2 - 2z^2) \cdot z}{48(x^2 + y^2 + z^2)^{7/2}} \end{cases} \quad (16)$$

(2) Motion equilibrium equation of particles

The forces acting on Fe-based fine particles in the composite field composed of flow field, magnetic field, and gravity field mainly include gas drag force, gravity force, Brownian force, and magnetic dipole force, and the motion equation of the particles in the three-dimensional space is expressed as below [36]:

$$\begin{cases} m_p \frac{d^2x}{dt^2} = F_{Dx} + F_{Mx} + F_{Bx} \\ m_p \frac{d^2y}{dt^2} = F_{Dy} + F_{My} + F_{By} \\ m_p \frac{d^2z}{dt^2} = F_{Dz} + F_{Mz} + F_{Bz} - m_p g \end{cases} \quad (17)$$

where F_{Dx} , F_{Mx} , and F_{Bx} are the drag force on particles, the magnetic dipole between particles, and the Brownian force they bear along the X axis, N; F_{Dy} , F_{My} , and F_{By} are the drag force on particles, the magnetic dipole between particles, and the Brownian force along the Y axis, N; F_{Dz} , F_{Mz} , and F_{Bz} are the drag force, the magnetic dipole between particles, and the Brownian force on particles along the Z axis, N.

(3) Calculation method of coagulation coefficient

Figure 5 shows the motion trajectory of particle j relative to core particle i in three-dimensional space from different initial positions in space, and all relative initial positions where particle j can collide with core particle i in unit time are determined. In this case, such initial position points $((x_{j0}, y_{j0}, z_{j0}), (x_{j1}, y_{j1}, z_{j1}), \dots, (x_{jn}, y_{jn}, z_{jn}))$ constitute an effective collision scope in the three-dimensional space, and its volume is the coagulation coefficient between particles i and j .

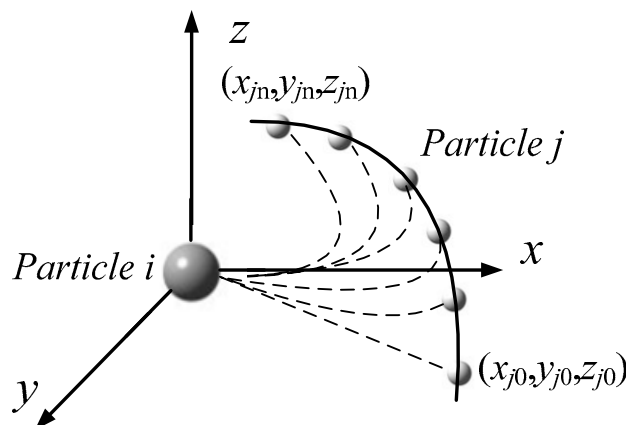


Figure 5. Schematic diagram of relative motion of two particles.

3.3. Calculation of the Magnetic Coagulation of Fe-Based Fine Particles Based on CFD-PBM

When calculating the magnetic coagulation process of particles in the composite field composed of flow field, magnetic field, and gravity field based on CFD-PBM, the coagulation cores of all coagulation types of particles in the flow field can be introduced into the PBM model in the form of UDF for calculation, and then the particle equilibrium equation can be solved by the partition method. For the magnetic coagulation core of Fe-based fine particles in a magnetic field, Kumar [37] has proposed the calculation formula for the magnetic coagulation core of particles in the free molecular zone and the continuous zone, as follows:

(1) Anisotropic magnetic coagulation core

$$\beta_{mag,co}^{sat} = \frac{2^{4/3}}{3^{7/6}} \left[\frac{m_i^{sat} m_j^{sat} \mu_0}{\pi} \right]^{1/3} (k_b T)^{2/3} \frac{1}{\mu} \frac{(d_i + d_j)}{d_i d_j} \tag{18}$$

$$\beta_{mag,fm}^{sat} = 3^{1/6} 2^{1/3} \left[\frac{m_i^{sat} m_j^{sat} \mu_0}{\pi} \right]^{1/3} (k_b T)^{1/6} \frac{1}{\rho_p^{1/2}} \left[\frac{1}{d_i^3} + \frac{1}{d_j^3} \right]^{1/2} (d_i + d_j) \tag{19}$$

(2) Isotropic magnetic coagulation core

$$\beta_{mag,co}^{sat} = \frac{2^{5/3}}{9} \left[\frac{m_i^{sat} m_j^{sat} \mu_0}{\pi} \right]^{1/3} (k_b T)^{2/3} \frac{1}{\mu} \frac{(d_i + d_j)}{d_i d_j} \tag{20}$$

$$\beta_{mag,fm}^{sat} = \frac{2^{2/3}}{3^{2/3}} \left[\frac{m_i^{sat} m_j^{sat} \mu_0}{\pi} \right]^{1/3} (k_b T)^{1/6} \frac{1}{\rho_p^{1/2}} \left[\frac{1}{d_i^3} + \frac{1}{d_j^3} \right]^{1/2} (d_i + d_j) \tag{21}$$

where T is the flow field temperature, K; m_i^{sat} and m_j^{sat} are the saturation magnetic moments of particle i and j , respectively, $A \times m^2$.

Whether particles are located in the free molecular zone or continuous zone can be judged according to $Kn = 2\lambda/d_p$ [14]; according to Allen and Raabe [38], the average free path λ of air is calculated as follows:

$$\lambda = \lambda_0 \frac{p_0}{p} \left(\frac{T}{T_0} \right)^2 \frac{T_0 + T_s}{T + T_s} \tag{22}$$

where $T_0 = 296.15$ K; $p_0 = 1.013 \times 10^5$ Pa; λ_0 is the average free path of air molecules at normal temperature and pressure, generally 67.3 nm; $T_s = 110.4$ K [38]; p is the absolute pressure of ambient gas, Pa; T is the absolute temperature of ambient gas, K. Through calculation, the size of particle Kn in the range of 0.5–2.5 μm is shown in Table 1.

Table 1. Kn value of particles of different diameters (300 K).

d_p (μm)	λ (nm)	Kn	C_c
0.5	68.41	0.2736	2.010
1.0	68.41	0.1368	1.933
1.5	68.41	0.09121	1.597
2.0	68.41	0.06841	1.438
2.5	68.41	0.05473	1.346

According to the size of Kn and the range in Table 2, the particles in the range of 0.5–1.0 μm belong in the near continuous zone/slip zone ($0.1 \leq Kn \leq 1$), and the particles in the range of 1.5–2.5 μm belong in the continuous zone ($0.01 \leq Kn \leq 0.1$). In order to simplify the study, the particles in the range of 0.5–1.0 μm also belong in the continuous zone.

Table 2. *Kn* value and region of particles of different diameters (300~2000 K).

d_p (μm)	0.01	0.1	1	10
<i>Kn</i>	10~100	1~10	0.1~1	0.01~0.1
Zone	Free molecular zone	Transition zone	Near-continuous zone/Slip zone	Continuous zone

After being determined, the magnetic coagulation kernel is added to the PBM model through UDF, the proton balance equation (PBE) or general dynamics equation (GDE) is solved to describe the evolution process of coagulation dynamics in the particle swarm equilibrium model, and its coagulation dynamics equation is as follows [39]:

$$\frac{dn(w, t)}{dt} = \frac{1}{2} \int_0^w \beta(w - v, v)n(w - v, t)n(v, t)dv - n(w, t) \int_0^\infty \beta(w, v)n(v, t)dv \quad (23)$$

where $n(w, t)$ is the particle number concentration distribution function of particles with a volume of w at time t , $((N/\text{m}^3)/\text{m}^3, N$ is the particle number); $\beta(w, v)$ is the coagulation kernel of two particles with volumes w and v , respectively, $(\text{m}^3/N)/\text{s}$; $1/2$ means that two particles simultaneously participate in one event of particle coagulation; the first term on the right side of the equation represents that the particle volume w is generated by the coagulation of particle volume (w, v) and particle volume v ; the second term on the right side of the equation indicates the particle volume w is lost by coagulation with other particles.

The partition method has the advantages of less calculated quantity, high calculation accuracy, flexible partition of subintervals, and simple coupling solving of the particle swarm equilibrium equation and two-fluid governing equation [40]. Therefore, the partition method was used to solve PBE, and then the whole coagulation process was numerically simulated, thus obtaining the time-dependent evolution process of the particle size distribution function. When the size of particles introduced from the inlet was $1.0 \mu\text{m}$, for example, the particle swarm was divided into eight intervals (Bin-7–Bin-0) during analog computation, where the particle coagulation direction in the flow field was Bin-7→Bin-6→Bin-5→Bin-4→Bin-3→Bin-2→Bin-1→Bin-0. When the ratio exponent was taken as 1.0 (the particle volume of the next interval and the particle volume of the previous interval satisfy $V_{k+1} = f_s V_k$, and $1.08 \leq f_s \leq 3.0$), the average particle size corresponding to each interval within Bin-7–Bin-0 was calculated as seen in Table 3. In addition, the average particle size from different inlets within Bin-7–Bin-0 is listed in Table 4.

Table 3. Average particle diameter in each interval from Bin-7 to Bin-0.

Interval Number	Average Particle Diameter (m)	Proportion (%)	Particle Volume Fraction (VF)
Bin-0	5.040×10^{-6}	0	0
Bin-1	4.000×10^{-6}	0	0
Bin-2	3.175×10^{-6}	0	0
Bin-3	2.520×10^{-6}	0	0
Bin-4	2.000×10^{-6}	0	0
Bin-5	1.587×10^{-6}	0	0
Bin-6	1.260×10^{-6}	0	0
Bin-7	1.000×10^{-6}	100	0.01420

Table 4. Average diameter in Bin-7 to Bin-0 subranges with different particle diameters of inlet.

Average Particle Diameter (μm)	Bin-7	Bin-6	Bin-5	Bin-4	Bin-3	Bin-2	Bin-1	Bin-0
Particle Diameter (μm)	d_7	d_6	d_5	d_4	d_3	d_2	d_1	d_0
0.5000	0.500	0.630	0.793	1.000	1.260	1.587	2.000	2.520
1.000	1.000	1.260	1.587	2.000	2.520	3.175	4.000	5.040
1.500	1.500	1.890	2.381	3.000	3.780	4.762	6.000	7.560
2.000	2.000	2.520	3.175	4.000	5.040	6.350	8.000	10.08
2.500	2.500	3.150	3.969	5.000	6.300	7.937	10.00	12.60

4. Simulation Correctness Verification

4.1. Grid Independence Test

In order to eliminate the influence of the number of grids on the numerical simulation, the grid independence test was carried out on the calculation model, and the optimal grid number was determined by calculating the collision probability between particles under different grid numbers. Due to the symmetry rule of the calculation area, the grid used in the calculation was a hexahedral structured grid, and the spherical wall of the core particle was refined. The calculation results are shown in Figure 6, with the increase in the number of grids, the magnetic coagulation removal efficiency first increased and then stabilized. When the number of grids increased from 270,000 to 650,000, the efficiency of magnetic coagulation removal changed to 0.5%. When the number of grids increased from 820,000 to 1,290,000, the efficiency of magnetic coagulation removal changed to 0.44%, and when the number of grids increased from 1,290,000 to 2,200,000, the efficiency of magnetic coagulation removal changed to 0.34%; that is, when the number of multi-fiber trapping structure grids reached about 650,000, the efficiency of magnetic coagulation removal remained basically unchanged. Therefore, 820,000 grids were selected for numerical simulation calculation.

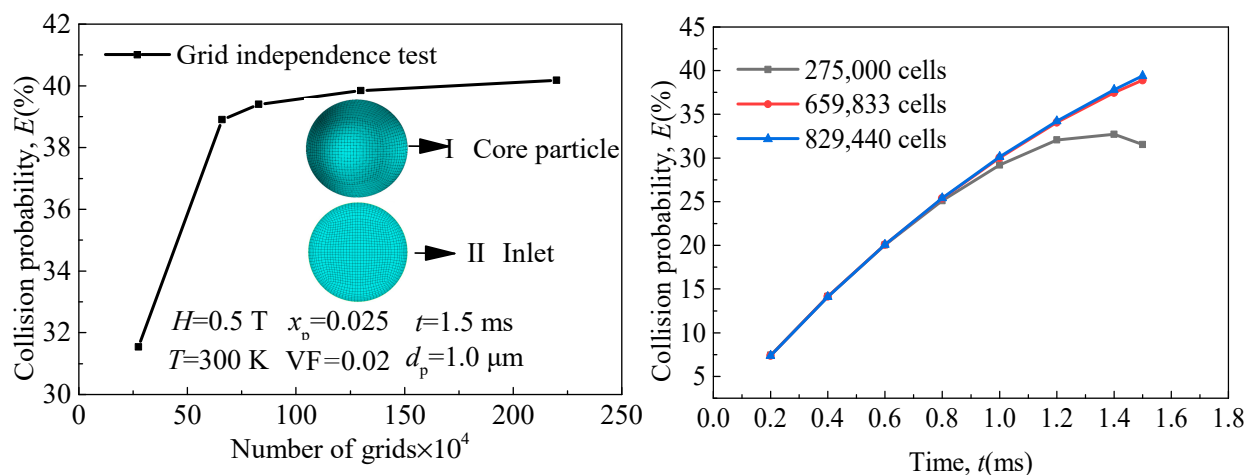


Figure 6. Grid independence test.

4.2. Experiment Verification of the Simulation Method

In order to verify the correctness of the numerical simulation method, the simulation was carried out under the same conditions as the particle collision experiment. The difference was that the collision in the experiment was between particles and droplets, but the collision mechanism was the same. Figure 7 shows the comparison between the numerical simulation value and the experiment value of particle collision probability. As shown in figure, Ranz and Wong [41] reported experiment values were higher than the simulation values, while those of Walton and Woolcock [42] and Schmidt and Loeffler [43] were close to the numerical simulation results, because the fluid Reynolds number in the Ranz and Wong experiment was much higher than the one in the numerical calculation model. In addition, the Langmuir and Blodgett theory value [44] and the Slinn [45] semi-

empirical formula calculation values were in good agreement with the changing trend of the numerical simulation results. The above results show that the numerical calculation model and method in this paper are suitable and can be used to calculate the particle collision probability.

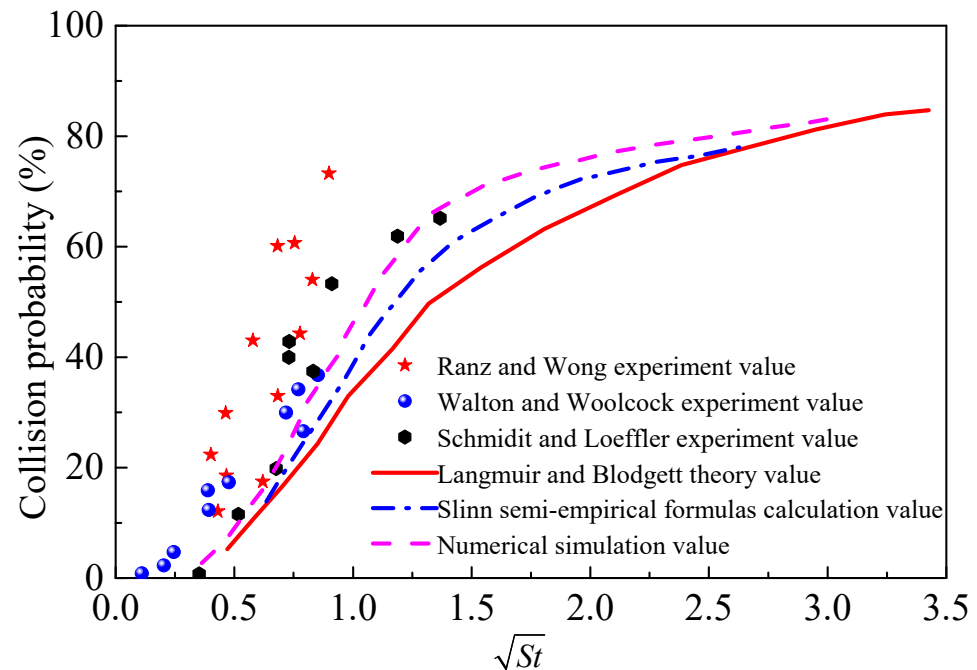


Figure 7. Comparison of numerical simulation value and experiment value of particle collision probability: Ranz and Wong [41]; Walton and Woolcock [42]; Schmidt and Loeffler [43]; Langmuir and Blodgett [44]; Slinn [45].

5. Numerical Simulation Calculation Results

5.1. Effect of Particle Size on Magnetic Coagulation Removal Efficiency of Fe-Based Fine Particles

Figure 8 shows the influence of the particle size on the magnetic coagulation of Fe-based fine particles in the composite field. As shown in the figure, the magnetic coagulation removal efficiency of Fe-based fine particles gradually increased with the change of residence time, and the larger the particle size, the worse the magnetic coagulation effect of Fe-based fine particles. When the particle size of Fe-based fine particles increased from 0.5 μm to 1.5 μm , the magnetic coagulation coefficient of Fe-based fine particles decreased from 0.5414 to 0.2882. This is because the larger the particle size is, the more difficult it is to change the motion state of particles, and the smaller the relative motion intensity between particles under the same magnetic dipole force. The magnetic coagulation coefficient of Fe-based fine particles presented a quadratic functional relationship with the particle size, and its formula is expressed as follows: $K = 0.7304 - 0.4196d_p + 0.0832d_p^2$. In addition, with the increase of the dust particle size, the magnetic coagulation strength of Fe-based fine particles under a random magnetic dipole orientation was greater than that under the aligned magnetic dipole orientation, and the difference between the magnetic coagulation removal efficiency under the random magnetic dipole orientation and that under the aligned magnetic dipole orientation was smaller.

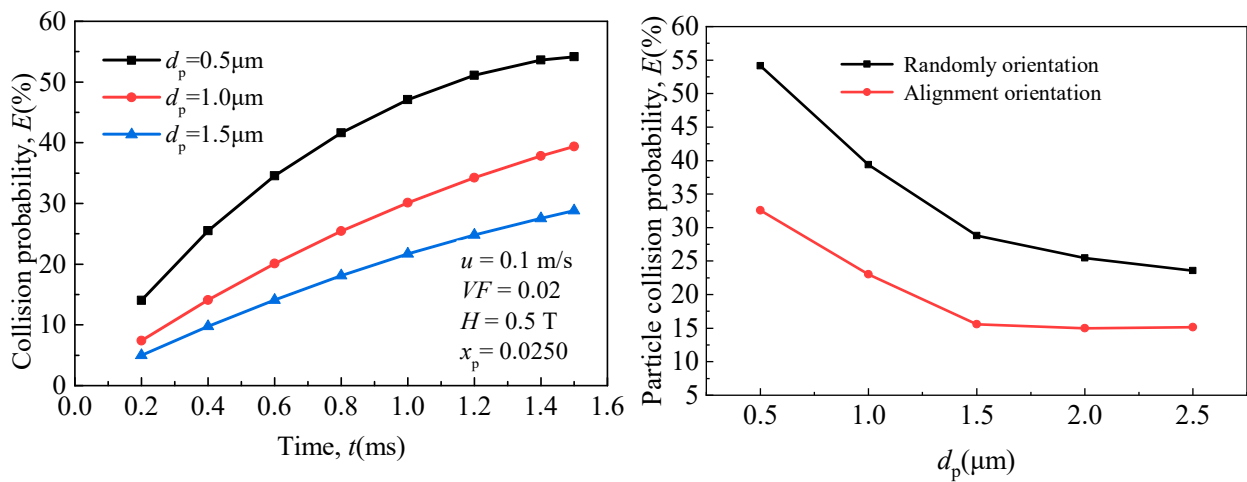


Figure 8. Effect of particle size on magnetic coagulation of Fe-based fine particles.

5.2. Effect of Particle Volume Fraction on Magnetic Coagulation Removal Efficiency of Fe-Based Fine Particles

Figure 9 shows the influence of the particle volume fraction on the magnetic coagulation of Fe-based fine particles in the composite field. As shown in the figure, the magnetic coagulation removal efficiency of Fe-based fine particles gradually increased with the change of residence time. The greater the particle volume fraction, the better the magnetic coagulation effect of Fe-based fine particles. When the particle volume fraction grew from 0.01 to 0.03, the magnetic coagulation coefficient of Fe-based fine particles increased from 0.2353 to 0.5061. The reason is that the increase of the particle volume fraction increases the number of particles in the composite field. Although the relative motion intensity of particles with the same particle size was unchanged under the same magnetic dipole force, the change in the quantity increased the probability of the collision between particles. The magnetic coagulation coefficient of Fe-based fine particles presented a quadratic functional relationship with the volume fraction, expressed as follows: $K = 0.0216 + 23.56VF - 247VF^2$. In addition, with the increase of the particle volume fraction, the magnetic coagulation strength of Fe-based fine particles under the random magnetic dipole orientation was greater than that under the aligned magnetic dipole orientation, and the difference between the magnetic coagulation removal efficiency under the random magnetic dipole orientation and that under the aligned magnetic dipole orientation was enlarged.

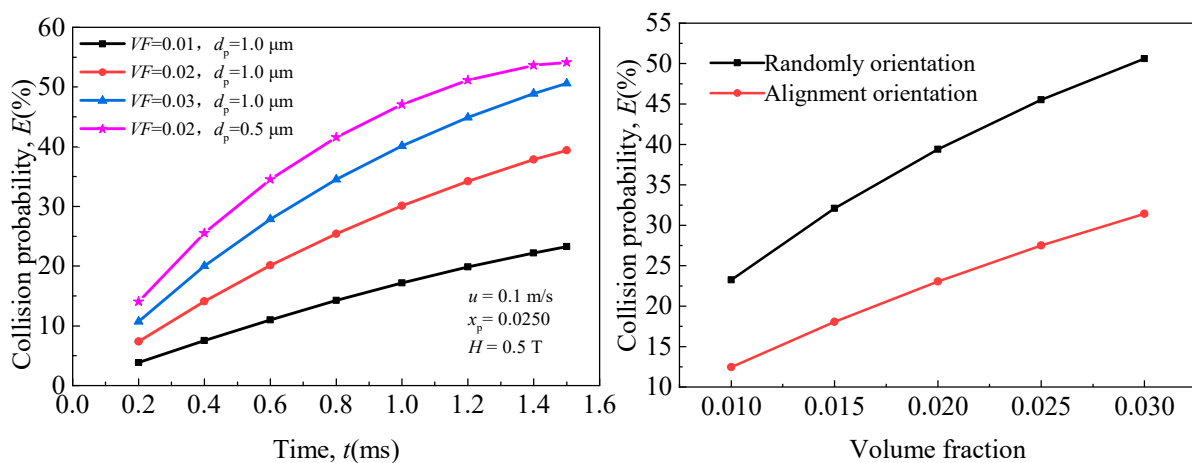


Figure 9. Effect of particle volume fraction on magnetic coagulation of Fe-based fine particles.

5.3. Effect of External Magnetic Field Strength on Magnetic Coagulation Removal Efficiency of Fe-Based Fine Particles

Figure 10 shows the influence of external magnetic field strength on the magnetic coagulation of Fe-based fine particles in the composite field. As shown in the figure, the magnetic coagulation removal efficiency of Fe-based fine particles gradually increased with the change of residence time. The greater the applied external magnetic field strength, the better the magnetic coagulation effect of Fe-based fine particles. When the applied external magnetic field strength increased from 0.5 T to 1.0 T, the magnetic coagulation coefficient of Fe-based fine particles increased from 0.3940 to 0.5288. This is because the greater the applied external magnetic field strength, the greater the magnetic dipole force between two particles after magnetization, and the greater the relative motion intensity of particles under the magnetic dipole force. The magnetic coagulation coefficient of Fe-based fine particles showed a quadratic functional relationship with the applied external magnetic field strength, expressed as follows: $K = 0.1808 + 10.096H - 62.72H^2$. In addition, as the applied external magnetic field strength increased, the magnetic coagulation strength of Fe-based fine particles under the random magnetic dipole orientation was greater than that under the aligned magnetic dipole orientation, and the difference between the magnetic coagulation removal efficiency under the random magnetic dipole orientation and that under the aligned magnetic dipole orientation remained basically unchanged.

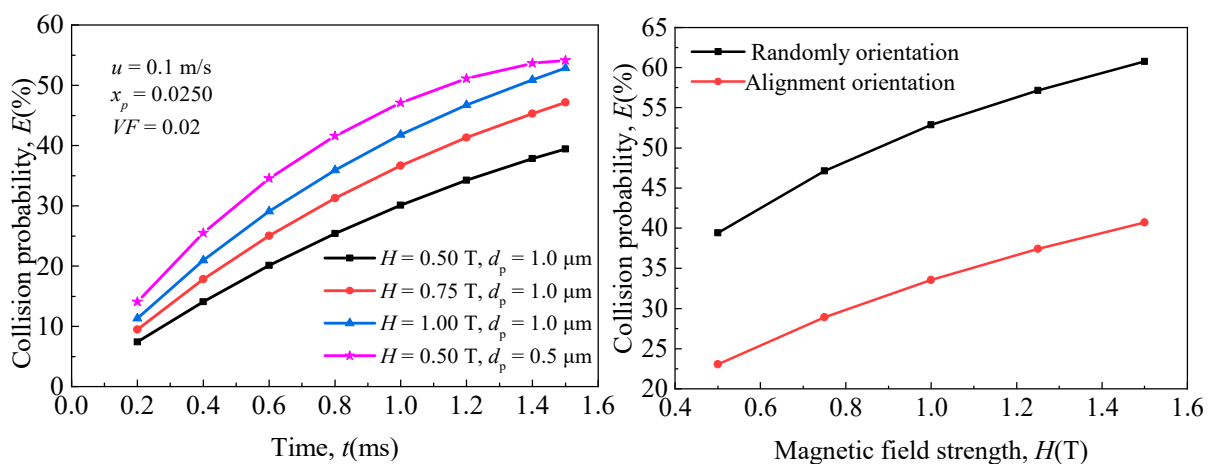


Figure 10. Effect of external magnetic field strength on magnetic coagulation of Fe-based fine particles.

5.4. Effect of Particle Magnetic Susceptibility on Magnetic Coagulation Removal Efficiency of Fe-Based Fine Particles

Figure 11 exhibits the influence of particle magnetic susceptibility on the magnetic coagulation of Fe-based fine particles in the composite field. As shown in the figure, the magnetic coagulation removal efficiency of Fe-based fine particles gradually increased with the change of residence time. The greater the particle magnetic susceptibility, the better the magnetic coagulation effect of Fe-based fine particles. When the magnetic susceptibility of Fe-based fine particles increased from 0.0250 to 0.0500, the coagulation coefficient of Fe-based fine particles increased from 0.3940 to 0.5288. This is because the greater the saturation magnetization of particles, the greater the magnetic dipole force between two particles after magnetization, and the greater the relative motion intensity of particles under the action of magnetic dipole force. The magnetic coagulation coefficient of Fe-based fine particles displayed a quadratic functional relationship with the magnetic susceptibility of particles, expressed as follows: $K = 0.1808 + 10.096x_p - 62.72x_p^2$. In addition, with the increase of particle magnetic susceptibility, the magnetic coagulation strength of Fe-based fine particles under the random magnetic dipole orientation was greater than that under the aligned magnetic dipole orientation, and the difference between the magnetic coagulation removal efficiency under the random magnetic dipole orientation and that under the aligned magnetic dipole orientation remained basically unchanged.

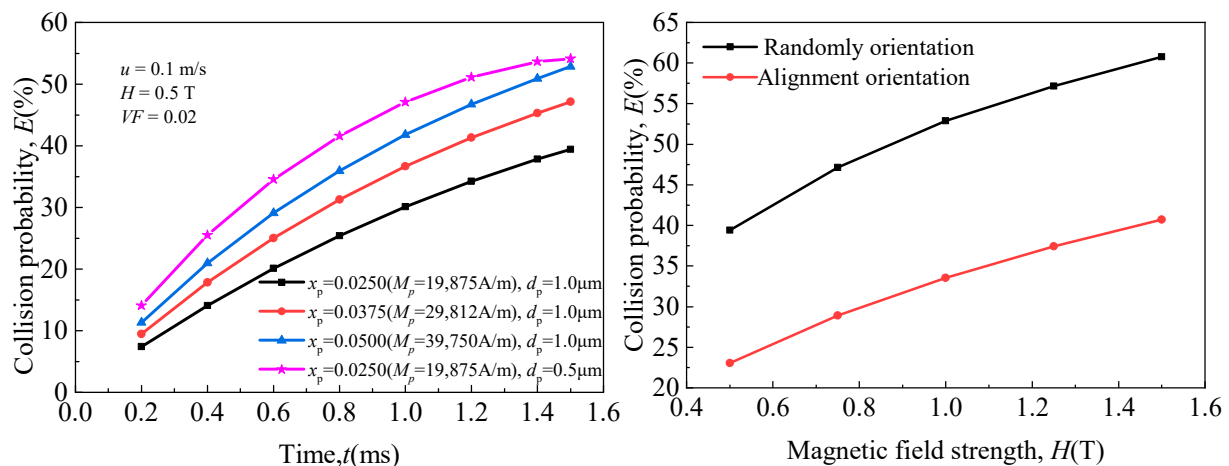


Figure 11. Effect of particle magnetic susceptibility on magnetic coagulation of Fe-based fine particles.

6. Conclusions

(1) The larger the particle size, the worse the coagulation effect of Fe-based fine particles. When the particle size of Fe-based fine particles increased from 0.5 μm to 1.5 μm , the magnetic coagulation coefficient of Fe-based fine particles decreased from 0.5414 to 0.2882. The multi-field coupling coagulation coefficient and the particle size of Fe-based fine particles satisfied a one-variable quadratic functional relationship as expressed by $K = 0.7304 - 0.4196d_p + 0.0832d_p^2$.

(2) The larger the particle volume fraction, the better the coagulation effect of Fe-based fine particles. As the particle volume fraction grew from 0.01 to 0.03, the magnetic coagulation coefficient of Fe-based fine particles increased from 0.2353 to 0.5061. The relationship between the magnetic coagulation coefficient of Fe-based fine particles and the particle volume fraction was a quadratic function, expressed as follows: $K = 0.0216 + 23.56VF - 247VF^2$.

(3) The greater the applied external magnetic field strength and particle magnetic susceptibility, the better the coagulation effect of Fe-based fine particles. When the applied external magnetic field strength increased from 0.5 T to 1.0 T or the magnetic susceptibility of Fe-based fine particles increased from 0.0250 to 0.0500, the magnetic coagulation coefficient of Fe-based fine particles increased from 0.3940 to 0.5288. The magnetic coagulation coefficient of Fe-based fine particles and their magnetic susceptibility conformed to a one-variable quadratic functional relationship, expressed as follows: $K = 0.1808 + 10.096H - 62.72H^2$, $K = 0.1808 + 10.096x_p - 62.72x_p^2$.

(4) The magnetic coagulation strength of Fe-based particles under a random magnetic dipole orientation was greater than that under the aligned orientation. As the dust particle size increased, the difference between the magnetic coagulation removal efficiency under the random magnetic dipole orientation and that under the aligned orientation became smaller, but the difference value was enlarged with the increase in the particle volume fraction. When the applied external magnetic field strength and particle magnetic susceptibility grew, the difference between the magnetic coagulation removal efficiency under the random magnetic dipole orientation and that under the aligned orientation basically unchanged.

Author Contributions: Conceptualization, methodology, formal analysis, and writing—original draft preparation, D.X.; methodology, supervision, and project administration, Z.H.; software, validation, and visualization, L.Z.; investigation, data curation, and editing, W.Z. All authors have read and agreed to the published version of the manuscript.

Funding: This work was supported by open fund for Key Laboratory of Industrial Dust Prevention and Control & Occupational Health and Safety, Ministry of Education (grant no. EK20211001), open fund for Joint National-Local Engineering Research Centre for Safe and Precise Coal Mining (grant no. EC2021017) and Scientific Research Foundation for High-level Talents of Anhui University of Science and Technology (grant no. 2023yjrc19).

Institutional Review Board Statement: Not applicable.

Informed Consent Statement: Not applicable.

Data Availability Statement: The datasets generated during and/or analyzed during the current study are available from the corresponding author on reasonable request.

Conflicts of Interest: The authors declare no conflict of interest.

Nomenclature

C_c	Cunningham correction factor
d_p	particle diameter, μm
F_B	Brownian force, N
F_D	drag force, N
F_g	gravity, N
f_s	interval particle volume, m^3
g	gravitational acceleration, m/s^2
Kn	particle Knudsen number
k_b	Boltzmann constant, 1.38×10^{-23} J/K
M_p	particle saturated magnetization, A/m
m_i	particle i magnetic dipole moment, $\text{A}\cdot\text{m}^2$
m_j	particle j magnetic dipole moment, $\text{A}\cdot\text{m}^2$
m_p	particle mass, kg
ρ_p	particle density, kg/m^3
Re	Reynolds number
S_0	noise spectral intensity, m^2/s^3
T	absolute temperature, K
t	time, s
u	fluid velocity, m/s
u_p	particle velocity, m/s
V_k	interval particle volume growth factor
μ_0	vacuum permeability, 1.256×10^{-6} N/A ²
Greek symbols	
α	volume fraction
θ	polar angle, rad
λ	air molecules average free path, nm
ν	fluid dynamic viscosity, Pa·s
ρ	fluid density, kg/m^3
Subscripts	
i	particle i
j	particle j
mag	magnetic field
sat	saturation magnetization

References

1. Lin, B.; Wu, R. Designing Energy Policy Based on Dynamic Change in Energy and Carbon Dioxide Emission Performance of China's Iron and Steel Industry. *J. Clean. Prod.* **2020**, *256*, 120412. [[CrossRef](#)]
2. Li, Q.; Wen, B.; Wang, G.; Cheng, J.; Zhong, W.; Dai, T.; Liang, L.; Han, Z. Study on Calculation of Carbon Emission Factors and Embodied Carbon Emissions of Iron-containing Commodities in International Trade of China. *J. Clean. Prod.* **2018**, *191*, 119–126. [[CrossRef](#)]
3. Feng, C.; Huang, J.; Wang, M. Analysis of Green Total-factor Productivity in China's Regional Metal Industry: A Meta-frontier Approach. *Resour. Policy* **2018**, *58*, 219–229. [[CrossRef](#)]

4. He, Z.; Guo, Q.; Wang, Z.; Li, X. Prediction of Monthly PM_{2.5} Concentration in Liaocheng in China Employing Artificial Neural Network. *Atmosphere* **2022**, *13*, 1221. [[CrossRef](#)]
5. Zhao, C.; Pu, W.; Niu, M.; Wazir, J.; Song, S.; Wei, L.; Li, L.; Su, Z.; Wang, H. Respiratory Exposure to PM_{2.5} Soluble Extract Induced Chronic Lung Injury by Disturbing the Phagocytosis Function of Macrophage. *Environ. Sci. Pollut. R.* **2022**, *29*, 13983–13997. [[CrossRef](#)]
6. Zhou, G.; Low, Z.; Feng, S.; Zhang, F.; Zhong, Z.; Xing, W. Effect of Relative Humidity and Dust Moisture Content on Filtration Performance of Bag Filter. *Sep. Purif. Technol.* **2023**, *308*, 122952. [[CrossRef](#)]
7. Hosseini, S.A.; Tafreshi, H.V. On the Importance of Fibers' Cross-sectional Shape for Air Filters Operating in the Slip Flow Regime. *Powder. Technol.* **2011**, *212*, 425–431. [[CrossRef](#)]
8. Bao, L.; Musadiq, M.; Kijima, T.; Kenmochi, K. Influence of Fibers on the Dust Dislodgement Efficiency of Bag Filters. *Text. Res. J.* **2014**, *84*, 764–771. [[CrossRef](#)]
9. Huang, H.; Wang, K.; Zhao, H. Numerical Study of Pressure Drop and Diffusional Collection Efficiency of Several Typical Noncircular Fibers in Filtration. *Powder Technol.* **2016**, *292*, 232–241. [[CrossRef](#)]
10. Kasper, G.; Schollmeier, S.; Meyer, J. Structure and Density of Deposits Formed on Filter Fibers by Inertial Particle Deposition and Bounce. *J. Aerosol. Sci.* **2010**, *41*, 1167–1182. [[CrossRef](#)]
11. Zhou, J.; Zhang, L.; Zhang, B.; Gong, W. Study on Filtration Performance of Elliptical Fiber with Different Arrangements. *J. Eng. Fiber. Fabr.* **2020**, *15*, 1–11. [[CrossRef](#)]
12. Fakron, O.M.; Field, D.P. 3D Image Reconstruction of Fiber Systems Using Electron Tomography. *Ultramicroscopy* **2015**, *149*, 21–25. [[CrossRef](#)] [[PubMed](#)]
13. Qian, F.; Huang, N.; Zhu, X.; Lu, J. Numerical Study of the Gas–solid Flow Characteristic of Fibrous Media Based on SEM Using CFD-DEM. *Powder Technol.* **2013**, *249*, 63–70. [[CrossRef](#)]
14. Li, W.; Shen, S.; Li, H. Study and Optimization of the Filtration Performance of Multi-fiber Filter. *Adv. Powder Technol.* **2016**, *27*, 638–645. [[CrossRef](#)]
15. Yue, C.; Zhang, Q.; Zhai, Z. Numerical Simulation of the Filtration Process in Fibrous Filters Using CFD-DEM Method. *J. Aerosol. Sci.* **2016**, *101*, 174–187. [[CrossRef](#)]
16. Shu, Z.; Qian, F.; Fang, C.; Zhu, J. Numerical Simulation of Particle Spatial Distribution and Filtration Characteristic in the Pleated Filter Media Using OpenFOAM. *Indoor Built Environ.* **2020**, *30*, 1159–1172. [[CrossRef](#)]
17. Cao, B.; Wang, S.; Dong, W.; Zhu, J.; Qian, F.; Lu, J.; Han, Y. Investigation of the Filtration Performance for Fibrous Media: Coupling of a Semi-analytical Model with CFD on Voronoi-based Microstructure. *Sep. Purif. Technol.* **2020**, *251*, 117364. [[CrossRef](#)]
18. Bucher, T.M.; Tafreshi, H.V.; Tepper, G.C. Modeling Performance of Thin Fibrous Coatings with Orthogonally Layered Nanofibers for Improved Aerosol Filtration. *Powder Technol.* **2013**, *249*, 43–53. [[CrossRef](#)]
19. Subrenat, A.; Bellettre, J.; Cloirec, P.L. 3-D Numerical Simulations of Flows in a Cylindrical Pleated Filter Packed with Activated Carbon Cloth. *Chem. Eng. Sci.* **2003**, *58*, 4965–4973. [[CrossRef](#)]
20. Dong, M.; Li, J.; Shang, Y. Numerical Investigation on Deposition Process of Submicron Particles in Collision with A Single Cylindrical Fiber. *J. Aerosol. Sci.* **2019**, *129*, 1–15. [[CrossRef](#)]
21. Huang, H.; Zheng, C.; Zhao, H. Numerical Investigation on Non-steady-state Filtration of Elliptical Fibers for Submicron Particles in the “Greenfield gap” Range. *J. Aerosol. Sci.* **2017**, *114*, 263–275. [[CrossRef](#)]
22. Nazaroff, W. Indoor Particle Dynamics. *Indoor Air* **2004**, *14*, 175–183. [[CrossRef](#)] [[PubMed](#)]
23. Guo, Y.; Gao, X.; Zhu, T.; Luo, L.; Zheng, Y. Chemical Profiles of PM Emitted from the Iron and Steel Industry in Northern China. *Atmos. Environ.* **2017**, *150*, 187–197. [[CrossRef](#)]
24. Jia, J.; Cheng, S.; Yao, S.; Xu, T.; Zhang, T.; Ma, Y.; Wang, H.; Duan, W. Emission Characteristics and Chemical Components of Size-segregated Particulate Matter in Iron and Steel Industry. *Atmos. Environ.* **2018**, *182*, 115–127. [[CrossRef](#)]
25. Hleis, D.; Fernández-Olmo, I.; Ledoux, F.; Kfoury, A.; Courcot, L.; Desmots, T.; Courcot, D. Chemical Profile Identification of Fugitive and Confined Particle Emissions from an Integrated Iron and Steelmaking Plant. *J. Hazard. Mater.* **2013**, *250–251*, 246–255. [[CrossRef](#)] [[PubMed](#)]
26. Zhang, L.; Diao, Y.; Jiang, J.; Chu, M.; Han, K.; Shen, H. Study on Turbulent Aggregation Dynamics in the Process of Fine Particles Capture by Single Fibers. *Particul. Sci. Technol.* **2023**, *41*, 222–230. [[CrossRef](#)]
27. Zhang, W.; Qi, H.; You, C.; Xu, X. Mechanical analysis of agglomeration and fragmentation of particles during collisions. *J. Tsinghua Univ. Sci. Technol.* **2002**, *42*, 1639–1643.
28. Ku, J.; Chen, H.; He, K.; Yan, Q. Simulation and Observation of Magnetic Mineral Particles Aggregating into Chains in a Uniform Magnetic Field. *Miner. Eng.* **2015**, *79*, 10–16. [[CrossRef](#)]
29. Ku, J.; Chen, H.; He, K.; Xu, L.; Yan, Q. Numerical Simulation of Agglomeration Process Dynamics of Ferromagnetic Mineral Particles in a Weak Magnetic Field. *Int. J. Miner. Process.* **2014**, *133*, 46–51. [[CrossRef](#)]
30. Ke, C.; Shu, S.; Zhang, H.; Yuan, H. LBM-IBM-DEM Modelling of Magnetic Particles in a Fluid. *Powder Technol.* **2017**, *314*, 264–280. [[CrossRef](#)]
31. Senkawa, K.; Nakai, Y.; Mishima, F.; Akiyama, Y.; Nishijima, S. Measurement of the Adhesion Force Between Particles for High Gradient Magnetic Separation of Pneumatic Conveyed Powder Products. *Physica C* **2011**, *471*, 1525–1529. [[CrossRef](#)]
32. Karvelas, E.G.; Lampropoulos, N.K.; Benos, L.T.; Karakasidis, T.; Sarris, I.E. On the Magnetic Aggregation of Fe₃O₄ Nanoparticles. *Comput. Meth. Prog. Bio.* **2021**, *198*, 105778. [[CrossRef](#)] [[PubMed](#)]

33. Hua, F.; Kang, Y.; Zhong, K. Influent of Turbulent Effect on the Collection Process of Aerosols by Raindrops. *China Environ. Sci.* **2017**, *37*, 13–20.
34. Dastoori, K.; Kolhe, M.; Mallard, C.; Makin, B. Electrostatic precipitation in a small scale wood combustion furnace. *J. Electrostat.* **2011**, *69*, 466–472. [[CrossRef](#)]
35. Fuchs, N.A.; Daisley, R.E.; Fuchs, M.; Davies, C.N.; Straumanis, M.E. The Mechanics of Aerosols. *Phys. Today* **1965**, *18*, 73. [[CrossRef](#)]
36. Li, Y.; Zhao, C.; Wu, X.; Lu, D.; Han, S. Aggregation Mechanism of PM₁₀ from Coal Combustion in Uniform Magnetic Field. *CIESC. J.* **2007**, *58*, 987–993.
37. Kumar, P.; Biswas, P. Analytical Expressions of the Collision Frequency Function for Aggregation of Magnetic Particles. *J. Aerosol. Sci.* **2005**, *36*, 455–469. [[CrossRef](#)]
38. Allen, M.D.; Raabe, O.G. Slip Correction Measurements of Spherical Solid Aerosol Particles in an Improved Millikan Apparatus. *Aerosol. Sci. Technol.* **1985**, *4*, 269–286. [[CrossRef](#)]
39. Zhao, H.; Zheng, C.; Xu, M. Multi-Monte Carlo Method for General Dynamic Equation Considering Particle Coagulation. *Appl. Math. Mech.* **2005**, *26*, 875–882.
40. Poon, J.M.H.; Immanuel, C.D.; Doyle, F.J.; Litster, J.D. A Three-dimensional Population Balance Model of Granulation with a Mechanistic Representation of the Nucleation and Aggregation Phenomena. *Chem. Eng. Sci.* **2008**, *63*, 1315–1329. [[CrossRef](#)]
41. Ranz, W.; Wong, J. Impaction of Dust and Smoke Particles on Surface and Body Collectors. *Ind. Eng. Chem.* **1952**, *44*, 1371–1381. [[CrossRef](#)]
42. Walton, W.; Woolcoke, A. The Suppression of Airborne Dust by Water Spray. *Int. J. Air Pollut.* **1960**, *3*, 129–153. [[PubMed](#)]
43. Schmidt, M.; Löffler, F. Experimental Investigations on Two-phase Flow Past a Sphere Using Digital Particle-image-velocimetry. *Exp. Fluids* **1993**, *14*, 296–304. [[CrossRef](#)]
44. Langmuir, I.; Blodgett, K.B. A mathematical investigations of water droplet trajectories. *AAF Technical. Rep.* **1946**, *29*, 8–20.
45. Slinn, W.G.N. Some approximations for the wet and dry removal of particles and gases from the atmosphere. *Water Air Soil Pollut.* **1977**, *7*, 513–543. [[CrossRef](#)]

Disclaimer/Publisher’s Note: The statements, opinions and data contained in all publications are solely those of the individual author(s) and contributor(s) and not of MDPI and/or the editor(s). MDPI and/or the editor(s) disclaim responsibility for any injury to people or property resulting from any ideas, methods, instructions or products referred to in the content.